Sensors & Diagnostics

ROYAL SOCIETY OF CHEMISTRY

PAPER

View Article Online
View Journal | View Issue

Check for updates

Cite this: *Sens. Diagn.*, 2025, **4**, 884

Deciphering target-binding selectivity of waste printed circuit board-derived carbon nanozymes for pyrophosphate sensing

Kai-Yu Zheng,[a] Jia-Wei Kuo,[b] Cheng-Yan Yeh,[a]
Yang-Wei Lin[a] and Chong-You Chen*[b]

Received 20th May 2025,
Accepted 16th July 2025

DOI: 10.1039/d5sd00070j

rsc.li/sensors

Developing nanozyme-based sensors enables the upcycling of waste printed circuit boards (WPCBs) into functional sensing materials, offering both environmental sustainability and practical analytical capabilities. However, unlike natural enzymes with inherent target recognition, nanozymes often lack molecular selectivity, limiting their broader sensing applications. Moreover, developing waste-derived nanozymes with target recognition abilities presents considerable obstacles due to their uncontrolled and underexplored surface functionalities. In this study, we developed pyrophosphate (PPi)-responsive carbon nanozymes (CNZs) derived from WPCBs and investigated their intrinsic target-binding behavior. The peroxidase-mimicking CNZs were synthesized *via* simple carbonization of non-metallic fractions of WPCBs, followed by refluxing in alkaline solutions. Notably, the peroxidase-mimicking activity of CNZs was significantly suppressed by PPi, an important anionic biomarker in physiological processes and disease monitoring. Kinetic studies and comparative assays revealed the inhibition mechanism underlying the unique interaction between PPi and WPCB-derived CNZs. Upon the H_2O_2–CNZ complex formation, PPi subsequently interacts with the active carbonyl sites (C═O) on the CNZ surface, resulting in target-responsive inhibition. Built upon this unique binding behavior, the CNZ-based system achieved highly sensitive and selective colorimetric PPi sensing with a detection limit of 8.7 nM, with negligible interference even from structurally similar phosphate analogs. This work not only demonstrates the feasibility of converting waste into functional enzyme mimics, but also highlights a strategy for achieving intrinsic molecular selectivity in nanozyme-based sensors without relying on external recognition elements.

1. Introduction

Nanozymes, synthetic catalysts that mimic the functions of natural enzymes, have gained significant attention due to their superior stability, cost-effectiveness, and scalable production capabilities.[1,2] These engineered nanostructures are designed to perform a wide range of enzymatic activities, enabling diverse applications in biomedical sensing, imaging, cancer therapeutics, and environmental remediation.[3,4] Due to their customizable material properties, nanozymes offer substantial benefits over traditional catalytic materials by providing significant signal amplification for advanced biosensing.[5,6] In targeting specific analytes, nanozyme-based sensors are often functionalized with biorecognition elements such as antibodies, aptamers, and oligonucleotides to tailor their activity toward particular analytes.[7,8] However, these surface modification approaches using dense biomolecules can largely increase the steric hindrance, block the catalytic sites, and diminish their activity.[9] Unlike natural enzymes that inherently recognize specific targets, nanozymes face substantial challenges in achieving target-specific binding selectivity. This intrinsic limitation highlights a critical area for further research and development, focusing on enhancing the precision with which these synthetic materials mimic the natural enzyme recognition capabilities of their biological counterparts.

Recently, several target-responsive nanozymes have been reported to rely on their surface interactions with particular analytes, including metal nanomaterials,[10] metal–organic frameworks,[11] single-atom nanozymes,[12–14] nanozymatic carbon dots,[15–18] and supramolecular bionanozymes.[19] For instance, Li *et al.* improved the selectivity of iron-doped carbon dot nanozymes using an energy-governed electron lock that modulates the conduction band location to control electron transfer.[18] Zhang *et al.* demonstrated that using Ni as the binding site and the β-C ligand to facilitate oxygen reduction can effectively construct a selective uric acid

---

[a] *Department of Chemistry, National Changhua University of Education, Changhua City 50007, Taiwan*
[b] *Department of Chemistry, National Taiwan Normal University, Taipei 11677, Taiwan. E-mail: jasoncyc@ntnu.edu.tw*

oxidase-mimicking nanozyme.[14] In recent years, our group has focused on developing approaches for manipulating nanozyme selectivity using amino acids. For example, we have employed histidine to tailor the surface functional groups of nanozymatic carbon dots, thereby enabling precise binding to pyrophosphate ions.[15] This approach can lead to the development of highly sensitive and selective sensors for detecting alkaline phosphatase activity.[16] Most recently, we pioneered a rational supramolecular strategy using tryptophan as the recognition element, which has successfully brought about the creation of a human serum albumin-responsive bionanozyme.[19] While there have been remarkable advances in enhancing nanozyme targeting and selectivity, most existing synthesis methods still rely heavily on the use of extensive chemical reagents, complex procedures, and resource-intensive manufacturing, raising concerns about sustainability. In contrast, the concept of directly converting waste into functional nanozymes remains largely unexplored, especially in achieving target-specific recognition. Moreover, with the growing global demand for environmentally friendly and economically viable technologies, there is an urgent need to transition toward greener and more sustainable practices. Prioritizing the concepts of circular economy and urban mining, reclaiming raw precursors from waste offers a promising path forward.[20,21] However, developing waste-derived nanozymes with target recognition abilities presents considerable obstacles due to their uncontrolled and underexplored surface functionalities. This underscores the need for innovative and green chemistry that not only enables the fabrication of waste-derived nanozymes but also provides a deeper understanding of their interfacial interactions with specific targets.

Waste printed circuit boards (WPCBs) are one of the fastest-growing types of electronic waste worldwide and pose significant environmental and health issues for sustainable development.[22,23] Extracting materials from recycled WPCBs can conserve natural resources, thereby supporting sustainable economic and environmental benefits. WPCBs generally consist of 30% metallic fractions and 70% non-metallic fractions.[24] Metallic fractions are actively and easily recycled for the preparation of high-value products.[25] In contrast, non-metallic fractions (NMFs) primarily comprise epoxy resin, glass fibers, and flame retardants.[26] The thermosetting plastic properties of NMFs increase the difficulty and cost of recycling through chemical methods. They were usually discarded in landfills or used as low-cost fillers in industries.[27] Therefore, environmentally friendly and economically attractive recycling of NMFs can make significant progress in sustainable technologies. Several studies have utilized NMFs as precursors to synthesize useful products, including chemicals, fuels, carbon-based adsorbents, and supercapacitors.[28–32] For instance, Ma *et al.* produced phenolic compounds from NMFs by co-pyrolysis with waste tires.[30] Shen *et al.* converted NMFs to syngas for use as fuel.[31] Li *et al.* prepared hierarchical porous carbon through the carbonization of WPCBs for applications in supercapacitors.[32] Nevertheless, despite these significant efforts, the conversion of WPCBs into advanced carbon-based materials with incomparable characteristics and distinctive functionalities remains poorly explored. This is particularly noteworthy as waste-derived carbon nanozymes (CNZs) have recently garnered much interest due to their eco-friendly nature, high structural stability, and abundance of active sites.[33,34] Various waste materials, such as agricultural residues,[35–37] plant biomass,[38–41] and waste food,[42] have been used as carbon sources for CNZs. On the other hand, carbon dots, another family of carbon nanomaterials, have been prepared from several thermosoftening plastics for fluorescence applications.[43–45] However, the thermosetting plastics of WPCBs remain a particularly untapped resource for carbon nanozymes. Moreover, most waste-derived carbon nanozymes used as sensors are primarily effective for redox-related analytes, relying on their catalytic redox reactions.[35–42] This inherent deficiency in target binding selectivity significantly restricts their practical applications. Therefore, transforming the complex components of WPCBs into functionally selective nanozymes presents substantial barriers. These challenges stem not only from the complex nature of WPCBs but also from the limited understanding of utilizing their material properties for selective target binding. This complexity underscores the significant potential of waste-derived nanozyme technology to drive breakthroughs in analytical sensor development.

Pyrophosphate ($P_2O_7^{4-}$, PPi) is a key anionic species in biochemical processes, essential for various physiological functions and as a biomarker for disease monitoring.[46] It plays an important role in DNA synthesis, where PPi is a by-product of DNA polymerase reactions, allowing its concentration to serve as a vital indicator in real-time DNA sequencing and cancer diagnostics.[47] Furthermore, PPi is central to regulating numerous physiological processes; it is synthesized, degraded, and transported within the body to support diverse biological metabolisms.[48] For example, PPi is crucial in blood coagulation, influencing the process through its role in activated human platelet secretion.[49] Furthermore, unnormal PPi levels are known to inhibit hydroxyapatite deposition, leading to bone mineralization disorders, such as hypophosphatasia.[50,51] They are also highly related to metabolic conditions associated with calcium pyrophosphate deposition disease, including osteoporosis, hemochromatosis, and hyperparathyroidism.[52] Given its important biological roles, developing a sensitive and convenient method for PPi detection is paramount in understanding biological mechanisms and enhancing clinical diagnostics.

In this work, we report WPCB-derived CNZs with intrinsic recognition capabilities and high selectivity for colorimetric detection of PPi. NMFs of WPCBs were first carbonized followed by refluxing under alkaline conditions to obtain CNZs as shown in Scheme 1A. The carbonization temperature significantly impacts the active site of carbonyl (C=O) group

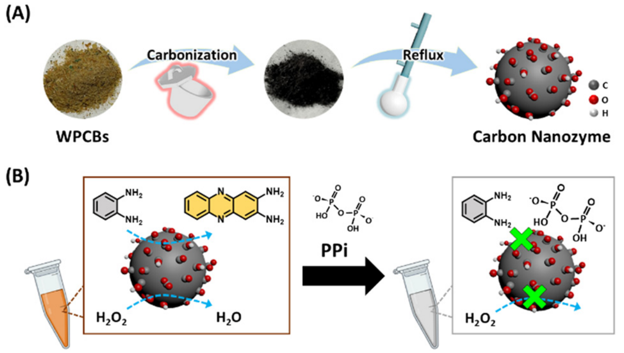

Scheme 1 Schematic illustration of (A) the PPi-responsive CNZ synthesized from WPCBs; (B) PPi induced the peroxidase-mimicking CNZ activity inhibition.

generation, which can regulate the CNZ catalytic activity. These peroxidase-mimicking CNZs can catalyze *o*-phenylenediamine (OPD) oxidation to produce a yellow product (2,3-diaminophenazine, DAP) when H_2O_2 is introduced. As demonstrated in Scheme 1B, the PPi addition subsequently leads to notable suppression of the CNZ peroxidase-mimicking activity. As compared with other catalysts, only CNZs display the PPi-induced inhibition effect. This finding suggests a specific interaction between CNZs and PPi even within the complex reaction mixture. To further clarify this interaction for responsive inhibition, kinetic analyses based on the Michaelis–Menten model are utilized to reveal the detailed mechanisms disrupting the reactions of H_2O_2 and OPD substrates individually. Building on these efforts, the PPi-responsive effect on WPCB-derived CNZ catalysis shows notable selectivity, successfully differentiating between urinary interference species and, particularly, other phosphate analogs. The remarkable recognition capability of the WPCB-derived CNZs enables highly sensitive and precise analysis of PPi using colorimetric methods to monitor inhibition efficiency, even in complex sample matrices. Our research demonstrates a sustainable strategy for engineering waste-derived nanozymes with intrinsic molecular selectivity, expanding their applicability in advanced biosensing and diagnostic platforms.

2. Experimental

2.1. Chemicals

Non-metallic fractions of WPCBs were provided by a local company. OPD, hydrogen tetrachloroaurate(III) trihydrate ($HAuCl_4 \cdot 3H_2O$), and sodium sulfate (Na_2SO_4) were purchased from Alfa Aesar (Lancashire, UK). Sodium nitrite ($NaNO_2$), sodium nitrate ($NaNO_3$), adenosine-5′-monophosphate (AMP), adenosine (Ado), and 2,2′-azino-bis(3-ethylbenzothiazoline-6-sulfonic acid) (ABTS) were purchased from Thermo Fisher Scientific (Waltham, USA). Sodium pyrophosphate tetrabasic decahydrate ($Na_4P_2O_7 \cdot 10H_2O$), bovine serum albumin (BSA), sodium acetate, sodium carbonate (Na_2CO_3), sodium phosphate (Na_3PO_4), and sodium urate were purchased from Sigma-Aldrich (St. Louis, MO, USA). Sodium hydroxide (NaOH), sodium chloride (NaCl), sodium bromide (NaBr), sulfuric acid (H_2SO_4), hydrochloric acid (HCl), nitric acid (HNO_3), and hydrogen peroxide (H_2O_2) were purchased from Showa (Tokyo, Japan). Glacial acetic acid and urea were purchased from J.T. Baker (Phillipsburg, USA). Adenosine 5′-triphosphate (ATP) and adenosine 5′-diphosphate (ADP) were purchased from Combi-Blocks (California, USA). Ethanol was obtained from Echo Chemical (Miaoli, Taiwan). Deionized water (>18.2 MΩ cm^{-1}) generated from an ELGA PURELAB classic system (Taipei, Taiwan) was used in all experiments.

2.2. Synthesis of WPCB-derived CNZs

CNZs were synthesized through carbonization of the non-metallic fractions followed by the refluxing method. To remove residual metals, WPCBs were first treated with freshly prepared *aqua regia* (HNO_3 : HCl = 1 : 3, v/v) for 30 min, followed by thorough washing with deionized water until the pH reached neutrality. The dried WPCBs (1 g) were typically carbonized in a furnace at 300 °C for 2 h. Carbonized powders (0.2 g) were mixed with 10 mL of 0.5 M NaOH and refluxed at 80 °C for 16 h. After cooling to room temperature, the mixture was centrifuged at 14 000 rpm for 10 min to remove large particles, and the resulting supernatant was collected. Ethanol was then added to the supernatant, and the precipitate was recovered by centrifugation at 5000 rpm for 3 min. The collected sediment was washed with ethanol five times. Finally, the purified CNZs were redispersed in deionized water and stored in the dark at 4 °C.

2.3. Material characterization

High-resolution transmission electron microscopy (TEM) images were obtained through a JEM-2100F field emission transmission electron microscope (JEOL, Tokyo, Japan). Fourier transform IR (FTIR) spectra were obtained from an FT/IR4600 FTIR spectrometer (JASCO, Tokyo, Japan). X-ray photoelectron spectroscopy (XPS) was conducted using a PHI Quantes spectrometer (ULVAC-PHI, Inc., Japan). A monochromatic Al Kα (1486.6 eV) light source with a total resolution of 0.2 eV and a beam size of 100 μm was maintained for measurements. UV-vis absorption spectra were acquired from a Cary 60 UV-vis spectrophotometer (Agilent Technologies, CA, USA). Fluorescence spectra were obtained from a Fluoromax Plus spectrometer (HORIBA, Kyoto, Japan). Dynamic light scattering (DLS) and ζ-potential measurements were performed using a Zetasizer Nano S instrument (Malvern Instruments Ltd., Malvern, UK).

2.4. PPi-induced inhibition on peroxidase-mimicking WPCB-derived CNZs

A mixture containing 100 μL of WPCB-derived CNZs (1 μg mL^{-1} in 0.1 M pH 4.0 acetate buffer), 100 μL of PPi with various concentrations (0.1 M pH 4.0 acetate buffer), 400 μL of OPD (80 mM in 5% DMSO/95% 0.1 M pH 4.0 acetate buffer), and 300 μL of 0.1 M pH 4.0 acetate buffer was thoroughly mixed. Subsequently, 100 μL of H_2O_2 (200 mM) was added to initiate the catalytic reaction, which proceeded for 1 h. The absorption spectra of reaction solutions were recorded, and the relative absorbance change ($\Delta A/A_0$) of the yellow-colored product at 450 nm was used for quantitative analysis of PPi concentration. Human urine (Golden West Biologicals, California, USA) was first filtered through a microporous membrane with a pore size of 0.22 mm, followed by centrifugation at 4000*g* for 10 min using a 3000 Da molecular weight cutoff membrane to remove large biomolecules and particles. The resulting filtrates were diluted 1500-fold and analyzed following the protocol described above.

For catalytic reactions using ABTS as the chromogenic substrate instead of OPD, 400 μL of ABTS (2.5 mM) was used, while all other experimental conditions remained unchanged. Additionally, horseradish peroxidase (HRP) and peroxidase-mimicking gold nanoclusters (AuNCs) were employed as alternative catalytic materials, following the same experimental procedures described above. In the HRP enzymatic test, 100 μL of HRP solution (80 ng mL^{-1}) replaced the CNZ solution, with all other experimental conditions unchanged. To synthesize AuNCs, 5 mL of an aqueous $HAuCl_4$ solution (10 mM) was rapidly added to 5 mL of BSA solution (50 mg mL^{-1}) under vigorous stirring at 37 °C. After 2 min, 0.5 mL of NaOH solution (1 M) was introduced, and the mixture was stirred vigorously for 12 h in the dark.[53] The solution color changed from yellow to dark brown, indicating successful AuNC formation. The resulting AuNC solution was stored at 4 °C in the dark until further use. For enzymatic activity tests, the AuNC solution was diluted tenfold with distilled water, and 100 mL of the diluted solution was used to replace the CNZ solution.

2.5. Steady-state kinetic study of peroxidase-mimicking WPCB-derived CNZs

The peroxidase-mimicking activity of WPCB-derived CNZs was assessed through the catalytic oxidation reactions of chromogenic substrates (OPD and ABTS) in the presence of H_2O_2. Various concentrations of OPD, ABTS, or H_2O_2 were separately reacted with CNZs under fixed experimental conditions, in the presence or absence of PPi, to evaluate the effect of PPi on the catalytic activity for each substrate. After a reaction of 1 h, the absorbance at 450 nm for OPD (420 nm for ABTS) was measured using UV-vis spectroscopy. The concentration of the oxidized chromogenic substrate was calculated using extinction coefficients of 16 700 M^{-1} cm^{-1} for OPD (36 000 M^{-1} cm^{-1} for ABTS) to measure the initial reaction rate. The apparent Michaelis–Menten constant (K_m^{app}) and the maximum initial velocity (V_{max}) values were determined from Lineweaver–Burk plots: $1/V = (K_m^{app}/V_{max})(1/[S]) + 1/V_{max}$, where V is the apparent initial velocity and [S] is the substrate concentration.

3. Results and discussion

3.1. Synthesis and characterization of WPCB-derived CNZs

As illustrated in Scheme 1A, WPCB-derived CNZs were prepared through carbonization of the non-metallic fractions at 300 °C for 2 h followed by refluxing WPCBs in an alkaline solution at 80 °C for 16 h. The morphology and size of WPCB-derived CNZs were characterized by TEM in Fig. 1A. The TEM image shows the spherical particle shape of CNZs, and the average particle size is calculated to be 3.4 ± 0.8 nm (n = 30). The high-resolution TEM image reveals that the crystalline structure of the CNZs exhibits a lattice spacing of 0.22 nm, corresponding to the (100) plane of graphite (inset of Fig. 1A).[54] The CNZ solution exhibits absorption below 300 nm, corresponding to π–π* transitions of aromatic sp^2 carbons, and between 300 and 400 nm, associated with n–π* transitions in the carbon core (Fig. 1B).[55] Additionally, Fig. 1B illustrates that the CNZs display a distinct fluorescence emission peak at 438 nm when excited at 310 nm. The fluorescence properties are excitation-wavelength-dependent, as demonstrated in Fig. S1. The emission wavelength red-shifts as the excitation wavelength increases from 300 to 490 nm (Fig. 1C). This fluorescence characteristic indicates that the synthesized nanomaterial exhibits a quantum confinement effect, similar to that observed in carbon nanomaterials derived from other waste sources.[34] These results of TEM images and

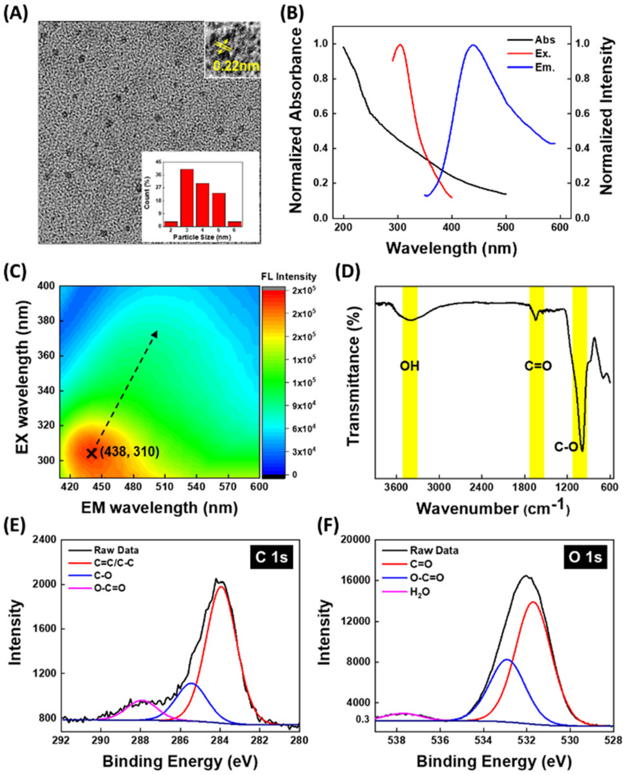

Fig. 1 Characterization of WPCB-derived CNZs. (A) TEM images. Inset: Particle size distribution. (B) Overlapping UV-vis absorption and fluorescence excitation/emission spectra. (C) Fluorescence excitation/emission mapping. (D) FTIR spectrum. Deconvoluted XPS spectra of (E) C 1s and (F) O 1s regions.

optical properties confirm the successful synthesis of WPCB-derived carbon nanomaterials.

To deeply delve into the material properties of CNZs, Fourier-transform infrared spectroscopy (FTIR) and X-ray photoelectron spectroscopy (XPS) were performed to analyze functional groups, element compositions, and surface oxidation states. In the FTIR spectrum (Fig. 1D), absorption bands at 3410 cm^{-1}, 1010 cm^{-1}, and 1650 cm^{-1} correspond respectively to the stretching vibrations of O–H, C–O, and C═O.[56–58] XPS analysis presented in Fig. S2 reveals that carbon (C 1s at 284.0 eV) and oxygen (O 1s at 532.2 eV) are the primary elements in the WPCB-derived CNZs, accompanied by additional signals from sodium (Na 1s at 1072 eV, Na KLL at 493 eV, Si 2s at 155 eV, and Si 2p at 102 eV). The deconvoluted spectra of C 1s, O 1s, Na 1s, and Si 2p are shown in Fig. 1 and S3. The high-resolution C 1s spectrum (Fig. 1E) displays peaks at 284.0, 285.5, and 288.0 eV, which are attributed to C–C/C═C, C–O, and O–C═O bonds, respectively.[59,60] In Fig. 1F, the high-resolution O 1s spectrum exhibits peaks at 531.7, 532.9, and 537.6 eV, associated respectively with C═O, O–C═O, and H_2O bonds.[61] The deconvoluted Na 1s spectrum shows a Na^+ peak due to the synthesis in alkaline solution, while the deconvoluted Si 2p spectrum reveals Si–O and Si–C bonds inherited from the glass fibers in the WPCBs (Fig. S3). The FTIR and XPS spectral analyses illustrate that the surface of the synthesized CNZs is rich in various oxygen-containing functional groups.

3.2. Transformation of WPCBs into peroxidase-mimicking CNZs

The peroxidase-mimicking properties of WPCB-derived CNZs were first investigated by performing benchmark catalytic reactions, as displayed in Fig. 2A. The CNZ-catalyzed reaction yields a yellow-colored product solution of DAP, exhibiting a distinct absorption peak at 450 nm (blue curve). When using CNZs (black curve) or H_2O_2 (red curve) alone, no significant change is observed in the absorbance of the OPD oxidation reaction mixtures. This indicates that the resulting WPCB-derived CNZs possess peroxidase-mimicking properties, catalyzing the oxidation of OPD upon the addition of H_2O_2 (Scheme 1B). In addition, we conducted catalysis at varying pH levels. As shown in Fig. S4 (black line), the peroxidase-mimicking activity of the CNZs is pH-dependent, with catalytic efficiency increasing under acidic conditions, similar to the natural enzyme HRP and other peroxidase-like nanozymes.[62,63] These tests suggest that WPCB-derived CNZs possess peroxidase-mimicking properties, catalyzing the oxidation of chromogenic substrates in the presence of H_2O_2.

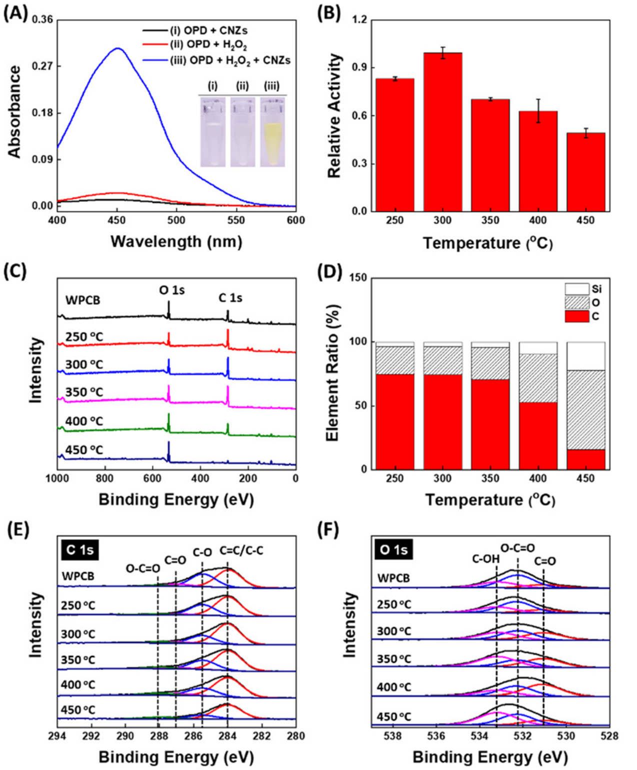

Fig. 2 Peroxidase-mimicking properties of WPCB-derived CNZs and chemical analysis of WPCBs at various carbonization temperatures. (A) Absorption spectra and photographs of OPD solutions (pH 4.0) in the presence of (i) CNZs alone (black curve), (ii) H_2O_2 alone (red curve), and (iii) both CNZs and H_2O_2. (B) Relative peroxidase-mimicking activity of CNZs prepared from WPCBs carbonized at different temperatures. The error bars indicate the standard deviation (n = 3). (C) XPS survey spectra, (D) elemental composition ratios, and deconvoluted (E) C 1s and (F) O 1s spectra of the WPCBs carbonized at various temperatures.

To understand the detailed top-down transformation of WPCBs into CNZs, the impact of carbonization temperatures was investigated on the peroxidase-mimicking activity. WPCBs were first carbonized at different temperatures ranging from 250 to 450 °C and then refluxed under the same conditions. The peroxidase-mimicking activity varied with carbonization temperature, achieving maximum catalytic efficiency at 300 °C, as displayed in Fig. 2B. SEM images show that the morphologies of WPCBs after carbonization at various temperatures exhibit no obvious changes in polymer–glass fiber composites (Fig. S5). In contrast, the chemical composition of the carbonized WPCBs changes with increasing temperatures, as revealed by XPS analysis in Fig. 2C. The XPS findings show that the carbon content varies with carbonization temperature, reaching a maximum of roughly 70% at 300 °C, and then gradually decreases as the temperature rises above 300 °C (Fig. 2D). The apparent decrease in carbon content might be attributed to the decomposition of phenolic resins, which produce gaseous products such as CO_2 at high carbonization temperatures.[64] In the high-resolution C 1s spectra shown in Fig. 2E, the amount of oxyhydrocarbons in the carbonized WPCBs decreases with elevating carbonization temperature. As displayed in the deconvoluted O 1s XPS spectra (Fig. 2F), the amount of C═O groups increases with carbonization temperature. According to previous studies, C═O groups serve as the catalytically active sites and chromogenic substrate binding sites for CNZs.[62,63] These results demonstrate that elevated carbon content and a higher concentration of C═O groups in the carbonized powders significantly improve the peroxidase-mimicking activity of CNZs at 300 °C.

After carbonization, the solid powders of carbonized WPCBs were treated by refluxing in an alkaline solution at 80 °C to create colloidal CNZs. Subsequent XPS analysis, as shown in Fig. S6, displays the survey spectra from this treatment, indicating that the main components remain unchanged. Additionally, high-resolution C 1s and O 1s spectra reveal an increase in O–C═O and C═O groups, along with the presence of H_2O, suggesting that the CNZs have a hydrophilic surface (Fig. S7). This improvement in dispersibility through refluxing facilitates the top-down transformation of waste PCBs into colloidal CNZs in aqueous solutions. Moreover, the FTIR spectrum of carbonized WPCBs in Fig. S6B shows additional absorption bands at around 3000–2850 $\mathrm{cm^{-1}}$ and 1400 $\mathrm{cm^{-1}}$, corresponding to C–H stretching and deformation vibrations, respectively.[32] The FTIR comparison reveals a significant decrease in C–H components, indicating that the refluxing process oxidized the carbon components, thereby increasing the hydrophilicity and improving colloidal dispersion. Under optimal conditions, WPCB-derived CNZs from several batches exhibited similar peroxidase-mimicking activity, with a relative standard deviation (RSD) of 3.2% (Fig. S8). These results demonstrate the high reproducibility of this straightforward top-down method.

3.3. PPi-responsive WPCB-derived CNZs

While greater catalytic activity enhances sensitivity *via* signal amplification,[6] the improved selectivity of nanozymes can effectively diminish interference from competing substances, thereby establishing a robust sensor for analytical purposes. Although PPi is not a typical target of native peroxidases, it specifically inhibits reactions catalyzed by WPCB-derived CNZs, underscoring their unique selectivity (Scheme 1B). In the CNZ-catalyzed reaction system, the addition of PPi was found to reduce the absorption at 450 nm, which corresponds to the reaction product DAP (Fig. 3A). As shown in Fig. S3 (red line), the presence of PPi results in the suppression across different pH conditions. The inhibition is notably more effective in acidic environments. When the OPD substrate is replaced with 2,2′-azino-bis(3-ethylbenzothiazoline-6-sulfonic acid) (ABTS) as the chromogenic substrate, a similar decrease in the absorption of the CNZ-catalyzed oxidation product solution is observed (Fig. 3B). Although OPD and ABTS possess different chemical structures, both substrates exhibit comparable PPi-induced suppression of the product generation. This finding suggests that the PPi-responsive inhibition is not mediated by interactions with the chromogenic substrates, but rather arises from a distinct binding affinity of PPi toward CNZs. On the other hand, we tested different catalysts to explore the effect of PPi on inhibiting CNZ catalysis under identical experimental conditions, as shown in Fig. 3C and D. Both horseradish peroxidase (HRP) and peroxidase-mimicking gold nanoclusters (AuNCs) can catalyze the OPD oxidation toward the DAP product, resulting in an absorption peak at 450 nm. However, the addition of PPi did not result in any observable inhibition in these catalytic reactions. These comparative tests demonstrate that the distinctive suppression effects of PPi are exclusive to the peroxidase-mimicking activity of WPCB-derived CNZs. This PPi-responsive specificity suggests the crucial role of the unique interaction between PPi and CNZs during the catalytic process.

In the complex mixture containing not only PPi and CNZs but also chromogenic substrates and H_2O_2, we employed kinetic analysis based on the Michaelis–Menten model to investigate the PPi-CNZ interactions. The reaction rates for OPD and H_2O_2 were individually measured in separate experiments, both before and after the addition of PPi, for each substrate. The kinetic parameters of CNZs, including the apparent Michaelis–Menten constant (K_m^{app}) and the maximum initial rate (V_{max}), were determined through the Lineweaver–Burk plot (Fig. S9). The K_m^{app} value indicates the binding affinity between the substrate and the nanozyme, and the V_{max} reflects the maximal reaction velocity for converting substrates to products. In the absence of PPi, the K_m^{app} and V_{max} of CNZs for the OPD substrate are calculated to be 25.4 (±0.2) $\mathrm{mM^{-1}}$ and 4.72 (±0.05) × 10^{-8} M $\mathrm{s^{-1}}$, respectively. With the addition of PPi, these values change to 53.5 (±1.3) $\mathrm{mM^{-1}}$ and 4.77 (±0.07) × 10^{-8} M $\mathrm{s^{-1}}$. The effects of PPi on the K_m^{app} and V_{max} values of CNZs for the OPD

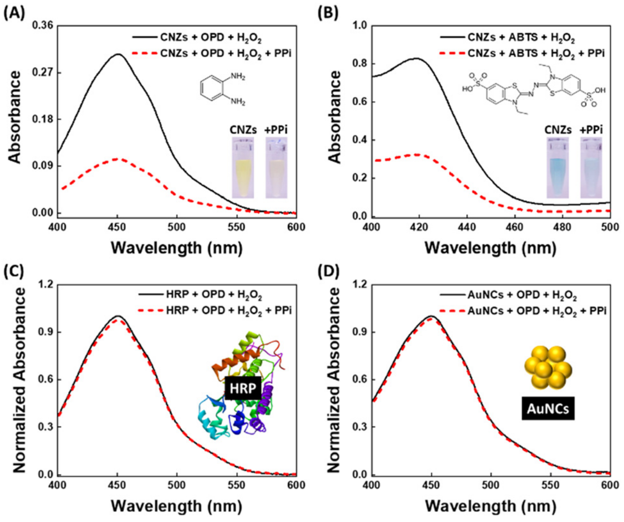

Fig. 3 Evaluation of PPi-induced inhibition based on absorption spectra. (A and B) Absorption spectra of CNZ-catalyzed reactions with H_2O_2 using (A) OPD and (B) ABTS as chromogenic substrates in the absence (black solid curve) and presence (red dashed curve) of PPi. (C and D) Absorption spectra of OPD and H_2O_2 reactions catalyzed by (C) HRP and (D) AuNCs in the absence (black solid curve) and presence (red dashed curve) of PPi. Insets: Chemical structures of chromogenic substrates and schematic illustration of catalytic materials used in comparative tests.

substrate are summarized in Fig. 4A. Similar results, with an obvious increase in K_m^{app} but relatively unchanged V_{max} values, induced by PPi for the chromogenic substrate ABTS, are also observed in Fig. S10. For the chromogenic substrates OPD and ABTS, which both undergo oxidation reactions, the similar V_{max} values accompanied by significantly increased K_m^{app} values indicate that PPi acts as a competitive inhibitor. This suggests that PPi and the chromogenic substrates bind at the same site, disrupting substrate affinity for CNZs, reducing enzyme–substrate complex formation, and consequently leading to decreased product generation. Previous studies have demonstrated that the C═O group on carbon nanozymes serves as the binding site for chromogenic substrates.[62,63] Therefore, our results suggest that the C═O group of CNZs represents the binding site for PPi, where it competes directly with chromogenic substrates.

In contrast, PPi causes different changes in the K_m^{app} and V_{max} values for the other substrate, H_2O_2, which undergoes a reduction reaction catalyzed by CNZs. Before addition of PPi, the K_m^{app} and the V_{max} of CNZs for H_2O_2 are 4.45 (±0.12) mM^{-1} and 1.48 (±0.02) $\times 10^{-8}$ M s^{-1}, respectively. After introduction of PPi, these values change to 1.88 (±0.03) mM^{-1} and 0.57 (±0.01) $\times 10^{-8}$ M s^{-1}. As shown in Fig. 4B, both K_m^{app} and V_{max} are significantly decreased by addition of PPi. This reveals that PPi functions as an uncompetitive inhibitor for the H_2O_2 substrate in the CNZ-catalyzed reaction. The uncompetitive inhibitor binds to a site distinct from the substrate active site and only when the enzyme–substrate complex is formed.[65] In this case, the uncompetitive inhibitor PPi binds to the CNZ–H_2O_2 complex, reducing the effective concentration of the complex available for product generation. This interaction leads to reductions in both decreased K_m^{app} and V_{max}, reflecting a decrease in the overall catalytic efficiency.

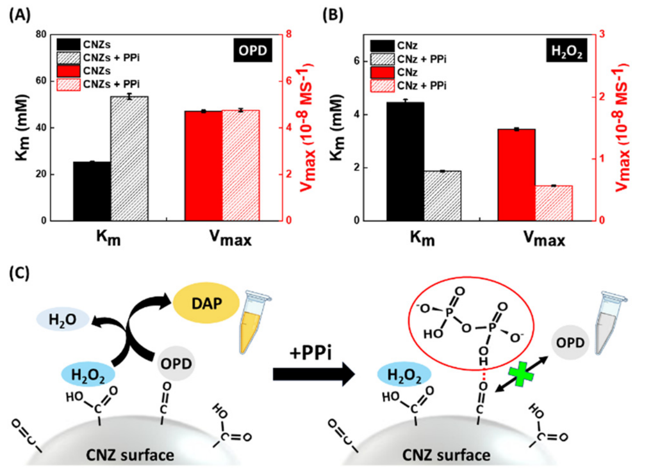

Fig. 4 PPi-induced inhibition mechanism study *via* steady-state kinetic analysis of CNZs. (A and B) Comparison of the apparent Michaelis–Menten constant (K_m^{app}, black) and the maximum initial rate (V_{max}, red) of CNZs for (A) OPD and (B) H_2O_2 substrates in the absence (solid bars) and presence (striped bars) of PPi. (C) Schematic illustration of the CNZ peroxidase-mimicking activity inhibition mechanism by PPi, which binds to the C═O site on the CNZ surface after the CNZ–H_2O_2 complex is formed. The error bars in all panels indicate the standard deviation (n = 3).

In summary, PPi functions as a competitive inhibitor for chromogenic substrates and as an uncompetitive inhibitor for H_2O_2 in the CNZ-catalyzed reaction system. These findings indicate that PPi binds to the same site on CNZs as the chromogenic substrates, thereby competing for chromogenic substrate interaction, and moreover, it specifically binds to the CNZ–H_2O_2 complex. In addition, previous studies report that the O–C═O group serves as the binding site for the H_2O_2 substrate, whereas the C═O group acts as the binding site for chromogenic substrates.[62,63] Drawing from these findings, the detailed mechanism of PPi-triggered suppression of WPCB-derived CNZ activity can be visualized in Fig. 4C. Initially, H_2O_2 binds to the O–C═O group to form the CNZ–H_2O_2 complex. Subsequently, PPi interacts with this complex by binding at the C═O site. The interaction of PPi with the CNZ surface not only reduces the binding affinity of chromogenic substrates but also decreases the catalytic conversion of the H_2O_2 substrate.

To further investigate the surface changes of CNZs involved in the inhibition mechanism, we measured their ζ-potential under different conditions (Fig. S11). The pristine CNZs exhibited a ζ-potential of −42.69 ± 3.91 mV, which can be attributed to the abundant surface O–C═O groups. Upon addition of PPi alone, the ζ-potential remained almost unchanged (−42.72 ± 1.23 mV), showing negligible interaction. Introduction of H_2O_2 alone slightly increased the surface ζ-potential to −39.68 ± 2.24 mV, suggesting the partial interaction of O–C═O groups with H_2O_2. Interestingly, when both H_2O_2 and PPi were added, the ζ-potential significantly decreased to −53.94 ± 2.21 mV. The results indicate that the negatively charged PPi binds to CNZs in the presence of H_2O_2. These surface changes are consistent with the proposed inhibition mechanism illustrated in Fig. 4C. It should also be noted that the surface changes during complex formation did not cause CNZ aggregation, as the hydrodynamic size showed no obvious change in the DLS results (Fig. S12A). Moreover, the fluorescence characteristics of CNZs were unaffected upon interaction with PPi and H_2O_2 (Fig. S12B), indicating that the binding does not perturb the emissive centers. To further explore the nature of the interaction between PPi and the C═O groups, a temperature-dependent study was performed (Fig. S13). As the temperature increased, the catalytic activity of CNZs was enhanced. However, the inhibition efficiency decreased at elevated temperatures, implying that the interaction between PPi and the C═O groups of CNZs is likely mediated by hydrogen bonding. These experiments support the proposed mechanism, in which PPi binding selectively disrupts substrate binding and subsequent catalytic conversion on the surface of the CNZ–H_2O_2 complex. As a result, the catalytic efficiency of WPCB-derived CNZs is significantly diminished in the presence of PPi. This interaction highlights the unique recognition capability of WPCB-derived CNZs and their potential to exhibit high selectivity toward specific targets.

3.4. Sensor performance of PPi-responsive WPCB-derived CNZs

Developing a straightforward colorimetric method with high selectivity and sensitivity for PPi detection is essential for facilitating early-stage diagnosis and treatment. The selectivity of PPi-responsive inhibition was evaluated through individually testing a variety of biological molecules under identical conditions, including urinary interference species and phosphate-containing molecules. As displayed in Fig. 5A, various possible interfering substances in urine were individually added into the CNZ-catalyzed reaction, such as Cl^-, Br^-, acetate, CO_3^{2-}, SO_4^{2-}, NO_3^-, NO_2^-, PO_4^{3-}, urea, and urate. A significant decrease in the absorption peak at 450 nm is observed only upon addition of PPi, indicating the noticeable suppression effect. The inhibition efficiency was assessed by the spectroscopic changes ($\Delta A/A_0$) as the signal response, where ΔA and A_0 represent the change in product absorbance at 450 nm with the addition and in the absence of the analyte, respectively. Fig. 5B shows that the PPi-triggered suppression is over 15 times stronger than that of interfering species. In biological samples such as urine, the concentrations of other phosphate analogs of Ado, including AMP, ADP, and ATP, are typically over 1000 times lower than that of PPi. Fig. 5C shows that these analogs, even at concentrations 10-fold lower than that of PPi and still above their physiological levels, have negligible effects on product absorbance at 450 nm. As demonstrated in Fig. 5D, the response to PPi is highly distinct and over 15 times stronger than that to other phosphate-containing species. This outstanding selectivity may be attributed to the steric hindrance caused by the adenosine moieties, which interferes with the pyrophosphate group binding to the C═O site on the CNZ–H_2O_2 complex.

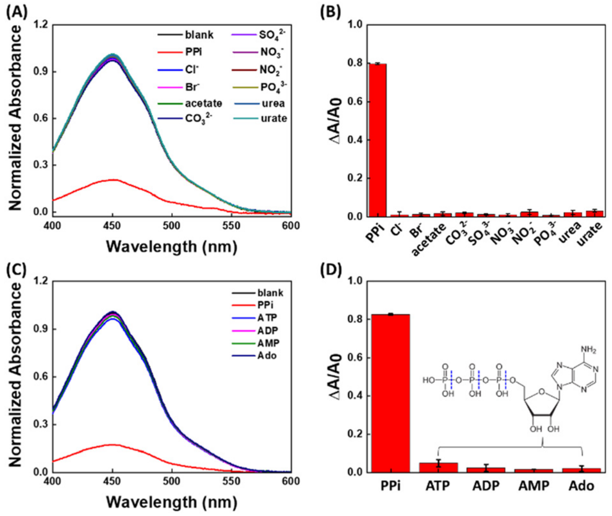

Fig. 5 Comparison of CNZ activity inhibition by PPi and other interfering species. (A and B) Absorption spectra (A) and absorbance changes at 450 nm ($\Delta A/A_0$) (B) of CNZs in the presence of PPi (10 μM) or urinary potential interfering substances (at the same concentration). (C and D) Absorption spectra (C) and absorbance changes at 450 nm ($\Delta A/A_0$) (D) of CNZs in the presence of PPi (10 μM) or phosphate analogs (1 μM). Inset: Chemical structures of the phosphate analogs. The error bars in all panels indicate the standard deviation (n = 3).

The nanozyme-engineered approach enables sensitive detection of PPi by monitoring PPi-responsive changes in CNZ activity. As the PPi concentration increased from 40 nM to 10 mM, the absorbance at 450 nm gradually decreased (Fig. 6A), reaching a plateau when the concentration is over 2 mM. The observation demonstrates that more PPi molecules competed with OPD substrates for the C═O groups on CNZs, leading to stronger catalytic suppression and a greater reduction in product formation. This concentration-dependent response allows for the construction of a calibration curve by plotting the spectroscopic response ($\Delta A/A_0$) with the added PPi concentration as depicted in Fig. 6B. The WPCB-derived CNZs exhibit a linear relationship between $\Delta A/A_0$ and the PPi concentration ($y = 1.1335x + 0.0122$, $R^2 = 0.9939$) within the range from 10 nM to 0.4 mM. The limit of detection is estimated to be 8.7 nM (signal-to-noise ratio = 3). The presented assay was compared to other recent methods for PPi detection, as displayed in Table 1. This represents the first PPi-responsive nanozyme sensor derived from WPCBs, demonstrating not only intrinsic selectivity but also excellent sensitivity, with strong potential for detecting micromolar-level PPi in real samples.

To evaluate the practicability of PPi determination in complex biological matrices, urine samples were subjected to simple filtration processes and diluted 1500-fold prior to analysis. The detected PPi concentration in the unspiked urine sample was 86.9 ± 3.4 μM. To further validate the accuracy and precision of the WPCB-derived CNZ sensor, recovery tests were performed by spiking known concentrations of PPi into urine samples, covering both normal and elevated concentration ranges observed in human urine.[72,73] After spiking 75, 150, and 225 μM PPi, the detected concentrations were 73.1 ± 2.1, 155 ± 2.2, and 232 ± 3.2 μM, respectively. As summarized in Table 2, recovery rates for PPi ranged from 97.5% to 103%, and the RSD values were lower than 4%, demonstrating distinguished analytical performance. The successful application of CNZs in PPi detection highlights their high selectivity and sensitivity,

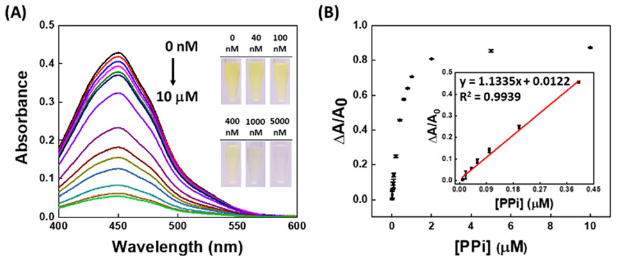

Fig. 6 (A) Inhibition of peroxidase-mimicking activity of WPCB-derived CNZs at varying concentrations of PPi. (B) Plot of the corresponding $\Delta A/A_0$ *versus* PPi concentration, where a good linear relationship is found in the calibration curve (inset). The error bars in all panels indicate the standard deviation (n = 3).

Table 1 Comparison of different optical methods for PPi detection

Material	Method	Phosphate analogs for the selectivity test	LOD	Ref.
Polymer	Fluorescence	PO_4^{3-}, PO_4^{2-}, PO_4^{-}	24 μM (4.2 ppm)	66
Carbon nanotubes	Fluorescence	PO_4^{3-}, ADP, ATP	4.4 μM	67
Polymer	Fluorescence	PO_4^{3-}, PO_4^{2-}, PO_4^{-}	87 nM (15.2 ppb)	68
Organic dye	Fluorescence	HPO_4^{2-}, $H_2PO_4^{-}$, $H_2PO_2^{3-}$	42.2 nM	69
Organic dye	Fluorescence	PO_4^{3-}, AMP, ADP, ATP	51 nM	70
Organic dye	Colorimetric	PO_4^{3-}, HPO_4^{2-}	250 μM	71
Waste-derived CNZs	Colorimetric	PO_4^{3-}, AMP, ADP, ATP	8.7 nM	This work

Table 2 Determination of PPi concentrations in urine samples

Spiked (μM)	Found (μM)	Recovery (%)	RSD (%, n = 3)
0	86.9 ± 3.4	—	3.95
75	73.1 ± 2.1	97.5	2.85
150	155 ± 2.2	103	1.41
225	232 ± 3.2	103	1.39

which enable precise and reliable analysis in biological samples. Notably, these CNZs were synthesized from WPCBs and exhibited performance characteristics suitable for practical sensing applications. The waste-derived nanozymes serve as a viable alternative to conventional sensing materials, supporting the advancement of next-generation diagnostic nanotechnologies.

Conclusions

We have successfully developed a straightforward strategy for synthesizing target-responsive CNZs from WPCBs, enabling a sensitive PPi sensing assay without the need for external recognition elements. The resulting CNZs exhibited remarkable PPi-responsive peroxidase-mimicking activity. Carbonization temperature was identified as a critical factor influencing catalytic performance by modulating both carbon content and surface oxidation states. Interestingly, PPi significantly and selectively inhibited the catalytic activity of CNZs, a distinctive phenomenon not observed with natural peroxidases or other nanozymes. Kinetic analyses revealed that this PPi-induced inhibition originates from the specific binding of PPi to the $C=O$ groups on the CNZ surface after the CNZ–H_2O_2 complex formation. This selective interaction competitively interferes with chromogenic substrate binding and simultaneously suppresses H_2O_2 conversion, markedly reducing CNZ catalytic activity. Importantly, this unique inhibition behavior provided exceptional selectivity toward PPi, even in comparison with structurally similar phosphate-containing molecules and common urinary interferences. Leveraging this target-responsive inhibition, a sensitive colorimetric PPi assay was developed, achieving a detection limit of 8.7 nM and enabling accurate quantification of micromolar-level PPi in urine samples without complicated pretreatments. This work represents a significant step toward developing target-selective nanozyme sensors derived from electronic waste, demonstrating that WPCB-based CNZs can serve as effective platforms for biochemical sensing and diagnostic applications.

Author contributions

Kai-Yu Zheng: investigation, methodology, data curation, formal analysis, validation. Jia-Wei Kuo: data curation, formal analysis, validation, writing – review & editing. Cheng-Yan Yeh: data curation, formal analysis. Yang-Wei Lin: supervision, writing – review & editing. Chong-You Chen: conceptualization, visualization, writing – original draft, writing – review & editing, supervision, funding acquisition.

Conflicts of interest

There are no conflicts to declare.

Data availability

Supplementary information is available, including fluorescence and XPS spectra, pH effect, SEM images, reproducibility tests, kinetic plots, zeta potential, hydrodynamic size distribution, and temperature effect analyses. See DOI: **https://doi.org/10.1039/D5SD00070J**.

All data supporting the findings of this study are available in the main text and the SI.

Acknowledgements

This work was supported by the Higher Education Sprout Project of National Taiwan Normal University (NTNU) and the National Science and Technology Council of Taiwan (NSTC 112-2113-M-003-020-MY2 and NSTC 111-2113-M-018-004-). The authors acknowledge Han-Pang Chen from the Instrument Center, College of Science, National Taiwan University/National Science and Technology Council for providing assistance in XPS measurements.

References

1 J. Wu, X. Wang, Q. Wang, Z. Lou, S. Li, Y. Zhu, L. Qin and H. Wei, *Chem. Soc. Rev.*, 2019, **48**, 1004–1076.
2 R. Zhang, X. Yan and K. Fan, *Acc. Mater. Res.*, 2021, **2**, 534–547.
3 Y. Chong, Q. Liu and C. Ge, *Nano Today*, 2021, **37**, 101076.

4 W. Gao, J. He, L. Chen, X. Meng, Y. Ma, L. Cheng, K. Tu, X. Gao, C. Liu, M. Zhang, K. Fan, D.-W. Pang and X. Yan, *Nat. Commun.*, 2023, **14**, 160.
5 M. Zandieh and J. Liu, *Adv. Mater.*, 2024, **36**, 2211041.
6 S. Li, Y. Zhang, Q. Wang, A. Lin and H. Wei, *Anal. Chem.*, 2022, **94**, 312–323.
7 Z. Xi, K. Wei, Q. Wang, M. J. Kim, S. Sun, V. Fung and X. Xia, *J. Am. Chem. Soc.*, 2021, **143**, 2660–2664.
8 Z. Wang, H. Chen, X. Cheng, Y. Wang, H. Wei, Z. Rong and S. Wang, *ACS Appl. Mater. Interfaces*, 2024, **16**, 44485–44492.
9 X. Chen, Y. Wang, X. Dai, L. Ding, J. Chen, G. Yao, X. Liu, S. Luo, J. Shi, L. Wang, R. Nechushtai, E. Pikarsky, I. Willner, C. Fan and J. Li, *J. Am. Chem. Soc.*, 2022, **144**, 6311–6320.
10 Y. Cong, R. Qiao, X. Wang, Y. Ji, J. Yang, D. Baimanov, S. Yu, R. Cai, Y. Zhao, X. Wu, C. Chen and L. Wang, *J. Am. Chem. Soc.*, 2024, **146**, 10478–10488.
11 M. Li, J. Chen, W. Wu, Y. Fang and S. Dong, *J. Am. Chem. Soc.*, 2020, **142**, 15569–15574.
12 Y. Wang, A. Cho, G. Jia, X. Cui, J. Shin, I. Nam, K.-J. Noh, B. J. Park, R. Huang and J. W. Han, *Angew. Chem., Int. Ed.*, 2023, **62**, e202300119.
13 X. Cao, C. Zhu, Q. Hong, X. Chen, K. Wang, Y. Shen, S. Liu and Y. Zhang, *Angew. Chem., Int. Ed.*, 2023, **62**, e202302463.
14 K. Wang, Q. Hong, C. Zhu, Y. Xu, W. Li, Y. Wang, W. Chen, X. Gu, X. Chen, Y. Fang, Y. Shen, S. Liu and Y. Zhang, *Nat. Commun.*, 2024, **15**, 5705.
15 C.-Y. Chen, Y. Z. Tan, P.-H. Hsieh, C.-M. Wang, H. Shibata, K. Maejima, T.-Y. Wang, Y. Hiruta, D. Citterio and W.-S. Liao, *ACS Sens.*, 2020, **5**, 1314–1324.
16 P. H. Hsieh, C. Y. Yeh, C. M. Wang, W. S. Liao and C. Y. Chen, *Chem. – Asian J.*, 2024, **19**, e202300878.
17 Y. Ouyang, Y. Biniuri, M. Fadeev, P. Zhang, R. Carmieli, M. Vázquez-González and I. Willner, *J. Am. Chem. Soc.*, 2021, **143**, 11510–11519.
18 G. Xu, K. Liu, B. Jia, Z. Dong, C. Zhang, X. Liu, Y. Qu, W. Li, M. Zhao, H. Zhou and Y.-Q. Li, *ACS Nano*, 2024, **18**, 3814–3825.
19 S.-Y. Chiang, C.-H. Peng, J.-W. Lin, J.-W. Kuo, Y.-W. Lin, C.-H. Lin and C.-Y. Chen, *ACS Appl. Mater. Interfaces*, 2025, **17**(14), 20693–20704.
20 P. Gautam, C. K. Behera, I. Sinha, G. Gicheva and K. K. Singh, *J. Cleaner Prod.*, 2022, **330**, 129836.
21 E. R. Rene, M. Sethurajan, V. Kumar Ponnusamy, G. Kumar, T. N. Bao Dung, K. Brindhadevi and A. Pugazhendhi, *J. Hazard. Mater.*, 2021, **416**, 125664.
22 Y. Chen, S. Liang, K. Xiao, J. Hu, H. Hou, B. Liu, H. Deng and J. Yang, *J. Cleaner Prod.*, 2021, **280**, 124505.
23 M. Baniasadi, F. Vakilchap, N. Bahaloo-Horeh, S. M. Mousavi and S. Farnaud, *J. Ind. Eng. Chem.*, 2019, **76**, 75–90.
24 A. K. Moe, J. Chungprempree, J. Preechawong, P. Sapsrithong and M. Nithitanakul, *Polymers*, 2023, **15**, 2938.
25 L. Pietrelli, S. Ferro and M. Vocciante, *Renewable Sustainable Energy Rev.*, 2019, **112**, 317–323.
26 A. Canal Marques, J.-M. Cabrera and C. de Fraga Malfatti, *J. Environ. Manage.*, 2013, **131**, 298–306.
27 P. Hadi, M. Xu, C. S. K. Lin, C.-W. Hui and G. McKay, *J. Hazard. Mater.*, 2015, **283**, 234–243.
28 Y. Kan, Q. Yue, J. Kong, B. Gao and Q. Li, *J. Chem. Eng.*, 2015, **260**, 541–549.
29 C. Ma, S. Kumagai, Y. Saito, T. Kameda, A. Watanabe, C. Watanabe, N. Teramae and T. Yoshioka, *ACS Sustainable Chem. Eng.*, 2022, **10**, 14775–14782.
30 C. Ma, S. Kumagai, Y. Saito, T. Kameda and T. Yoshioka, *Green Chem.*, 2021, **23**, 6392–6404.
31 Y. Shen, R. Yuan, X. Chen, X. Ge and M. Chen, *ACS Sustainable Chem. Eng.*, 2018, **6**, 9086–9093.
32 X. Du, L. Wang, W. Zhao, Y. Wang, T. Qi and C. M. Li, *J. Power Sources*, 2016, **323**, 166–173.
33 A. Das, R. V. S. Uppaluri and S. Mitra, *Chem. Eng. J.*, 2025, **507**, 160762.
34 T. C. Wareing, P. Gentile and A. N. Phan, *ACS Nano*, 2021, **15**, 15471–15501.
35 A. Saengsrichan, P. Khemthong, W. Wanmolee, S. Youngjan, J. Phanthasri, P. Arjfuk, P. Pongchaikul, S. Ratchahat, P. Posoknistakul, N. Laosiripojana, K. C. W. Wu and C. Sakdaronnarong, *Anal. Chim. Acta*, 2022, **1230**, 340368.
36 H. Ren, L. Yan, M. Liu, Y. Wang, X. Liu, C. Liu, K. Liu, L. Zeng and A. Liu, *Sens. Actuators, B*, 2019, **296**, 126517.
37 M. Wang, X. Zhou, S. Wang, X. Xie, Y. Wang and X. Su, *Anal. Chem.*, 2021, **93**, 3130–3137.
38 Q. Fang, Q. Liu, Y. Zhang and Y. Du, *Nanoscale*, 2023, **15**, 9718–9727.
39 C. J. Verma, P. Singh, R. P. Ojha and R. Prakash, *Mater. Adv.*, 2022, **3**, 2749–2759.
40 H. Ren, X. Liu, L. Yan, Y. Cai, C. Liu, L. Zeng and A. Liu, *Sens. Actuators, B*, 2020, **312**, 127979.
41 D. Bano, V. Kumar, V. K. Singh, S. Chandra, D. K. Singh, P. K. Yadav, M. Talat and S. H. Hasan, *ACS Sustainable Chem. Eng.*, 2019, **7**, 1923–1932.
42 A. F. Baye, M. W. Abebe and H. Kim, *Small*, 2024, **20**, 2402449.
43 B. Kommula, V. Gehlot, K. Kanwar, S. Sil, M. Banoo, A. Swarnkar, B. Rawat, K. Kailasam and U. K. Gautam, *Carbon*, 2025, **234**, 119960.
44 X. Zhou, J. Deng, Z. Li, Y. Cheng, J. Zhou, M. Jiang and W. Dong, *ACS Sustainable Chem. Eng.*, 2024, **12**, 16592–16602.
45 T. Kuang, M. Jin, X. Lu, T. Liu, H. Vahabi, Z. Gu and X. Gong, *Green Chem.*, 2023, **25**, 6581–6602.
46 S. K. Kim, D. H. Lee, J.-I. Hong and J. Yoon, *Acc. Chem. Res.*, 2009, **42**, 23–31.
47 S. Xu, M. He, H. Yu, X. Cai, X. Tan, B. Lu and B. Shu, *Anal. Biochem.*, 2001, **299**, 188–193.
48 R. A. Terkeltaub, *Am. J. Physiol.*, 2001, **281**, C1–C11.
49 S. A. Smith, S. H. Choi, R. Davis-Harrison, J. Huyck, J. Boettcher, C. M. Rienstra and J. H. Morrissey, *Blood*, 2010, **116**, 4353–4359.
50 A. M. Caswell, M. P. Whyte and R. G. G. Russell, *Crit. Rev. Clin. Lab. Sci.*, 1991, **28**, 175–194.
51 A. E. Timms, Y. Zhang, R. G. G. Russell and M. A. Brown, *Rheumatology*, 2002, **41**, 725–729.

52 C. Kleiber Balderrama, A. K. Rosenthal, D. Lans, J. A. Singh and C. M. Bartels, *Arthritis Care Res.*, 2017, **69**, 1400–1406.

53 J. Xie, Y. Zheng and J. Y. Ying, *J. Am. Chem. Soc.*, 2009, **131**, 888–889.

54 Y. H. Yuan, Z. X. Liu, R. S. Li, H. Y. Zou, M. Lin, H. Liu and C. Z. Huang, *Nanoscale*, 2016, **8**, 6770–6776.

55 G. Batra, S. Sharma, K. Kaushik, C. Rao, P. Kumar, K. Kumar, S. Ghosh, D. Jariwala, E. A. Stach, A. Yadav and C. K. Nandi, *Nanoscale*, 2022, **14**, 3568–3578.

56 D. R. d. S. Souza, J. P. d. Mesquita, R. M. Lago, L. D. Caminhas and F. V. Pereira, *Ind. Crops Prod.*, 2016, **93**, 121–128.

57 D. R. Da Silva Souza, L. D. Caminhas, J. P. de Mesquita and F. V. Pereira, *Mater. Chem. Phys.*, 2018, **203**, 148–155.

58 S. Nayak, P. Das and M. K. Singh, *Colloid Interface Sci. Commun.*, 2021, **45**, 100537.

59 Y. Zhang, W. Gao, Y. Ma, L. Cheng, L. Zhang, Q. Liu, J. Chen, Y. Zhao, K. Tu, M. Zhang and C. Liu, *Nano Today*, 2023, **49**, 101768.

60 Q. Lian, Z. Uddin Ahmad, D. Gang, M. Zappi, D. Fortela, B. Fortela and R. Hernandez, *Chemosphere*, 2020, **248**, 126078.

61 W.-S. Zou, Y. Xu, W. Kong, Y. Wang, J. Zhang, W. Li and H.-Q. Yu, *Anal. Chem.*, 2023, **95**, 1985–1994.

62 H. Sun, A. Zhao, N. Gao, K. Li, J. Ren and X. Qu, *Angew. Chem., Int. Ed.*, 2015, **54**, 7176–7180.

63 H. Sun, Y. Zhou, J. Ren and X. Qu, *Angew. Chem., Int. Ed.*, 2018, **57**, 9224–9237.

64 P. Evangelopoulos, E. Kantarelis and W. Yang, *J. Anal. Appl. Pyrolysis*, 2015, **115**, 337–343.

65 D. L. Nelson, *Lehninger principles of biochemistry*, W.H. Freeman, New York, 4th edn, 2005.

66 S. Mondal and N. Dey, *J. Environ. Chem. Eng.*, 2024, **12**, 114412.

67 S. Settele, C. A. Schrage, S. Jung, E. Michel, H. Li, B. S. Flavel, A. S. K. Hashmi, S. Kruss and J. Zaumseil, *Nat. Commun.*, 2024, **15**, 706.

68 S. Mondal and N. Dey, *ACS Appl. Polym. Mater.*, 2024, **6**, 10242–10253.

69 C. Zhao, H. Xu, Y. Meng, Y. Wang, S. Shuang and C. Dong, *J. Mol. Liq.*, 2023, **391**, 123326.

70 Z. Yu, F. Wang, S. Lu and X. Chen, *Dyes Pigm.*, 2025, **241**, 112874.

71 F. Cui, G. Yin, R. Yang and X. Guo, *Spectrochim. Acta, Part A*, 2020, **241**, 118658.

72 F. Wang, C. Zhang, Q. Xue, H. Li and Y. Xian, *Biosens. Bioelectron.*, 2017, **95**, 21–26.

73 Y. Shi, J. Wang, K. Mu, S. Liu, G. Yang, M. Zhang and J. Yang, *Sensors*, 2021, **21**, 5538.